CrossMark

ORIGINAL ARTICLE

Positive and negative ionospheric responses to the March 2015 geomagnetic storm from BDS observations

Shuanggen Jin[1] · **Rui Jin[1]** · **H. Kutoglu[2]**

Abstract The most intense geomagnetic storm in solar cycle 24 occurred on March 17, 2015, and the detailed ionospheric storm morphologies are difficultly obtained from traditional observations. In this paper, the Geostationary Earth Orbit (GEO) observations of BeiDou Navigation Satellite System (BDS) are for the first time used to investigate the ionospheric responses to the geomagnetic storm. Using BDS GEO and GIMs TEC series, negative and positive responses to the March 2015 storm are found at local and global scales. During the main phase, positive ionospheric storm is the main response to the geomagnetic storm, while in the recovery phase, negative phases are pronounced at all latitudes. Maximum amplitudes of negative and positive phases appear in the afternoon and post-dusk sectors during both main and recovery phases. Furthermore, dual-peak positive phases in main phase and repeated negative phase during the recovery are found from BDS GEO observations. The geomagnetic latitudes corresponding to the maximum disturbances during the main and recovery phases show large differences, but they are quasi-symmetrical between southern and northern hemispheres. No clear zonal propagation of traveling ionospheric disturbances is detected in the GNSS TEC disturbances at high and low latitudes. The thermospheric composition variations could be the dominant source of the observed ionospheric storm effect from GUVI $[O]/[N_2]$ ratio data as well as storm-time electric fields. Our study demonstrates that the BDS (especially the GEO) observa-
tions are an important data source to observe ionospheric responses to the geomagnetic storm.

Keywords Ionospheric anomaly · Geomagnetic storm · TEC · BDS · GIM

1 Introduction

The Earth's ionospheric response to geomagnetic storms following intense solar activity, i.e., ionospheric storm, is one of the most significant topics for the understanding of ionospheric temporal–spatial variation and improving modeling and forecasting of the ionospheric activities. This is vital for radio communication, satellite navigation, radar detection and other systems, which use trans-ionospheric electromagnetic wave signals. It is expected that phase shift and amplitude fading will be induced during the propagation of electromagnetic waves in the Earth's ionosphere. The research about ionospheric response to geomagnetic storms is essential for the ionospheric correction of electromagnetic wave signals because the storm has a wide range effect and high occurrence rate. Geomagnetic storms, especially moderate storms (-100 nT < Dst < −50 nT), appear frequently even during solar minimum activity years and the following ionospheric storms could last from several hours to several days (Mendillo 1971; Strickland et al. 2001; Liu et al. 2010; Echer et al. 2011).

The research of ionospheric storm has been an important topic in Earth and space science since it was firstly detected and discussed in the mid-twentieth century (Martyn 1953; Sato 1956; Seaton 1956; Matsushita 1959). Now an overall picture of ionospheric storm morphology and its mechanism for explanation has been drown out by the efforts of pioneers in space science within the last decades. In different phases

✉ Shuanggen Jin
  sgjin@shao.ac.cn; sg.jin@yahoo.com

[1] Shanghai Astronomical Observatory, Chinese Academy of Science, Shanghai 200030, China

[2] Department of Geomatics Engineering, Bulent Ecevit University, Zonguldak 67100, Turkey

of the solar cycle, geomagnetic storms could be induced by different solar wind drivers, which are classified into three main types: corotating high-speed streams, inter-streams from coronal holes and transient flows induced by coronal mass ejections (Richardson and Cane 2012). The increased solar wind pressure compresses the Earth's magnetosphere initially and energetic particles precipitate into the lower thermosphere at high latitudes simultaneously. This can disturb the chemical, thermal and electrodynamic equilibrium of solar-terrestrial space system and leads to a series of anomaly variations in the thermosphere, ionosphere, plasmasphere and magnetosphere. As Earth's stratified atmosphere is closely coupled between different layers, ionospheric storm morphologies vary with complicated temporal–spatial features. The discussion of ionospheric storm morphologies falls into two categories: one is statistical analysis and the other is case study (Mannucci et al. 2005; Ding et al. 2008; Jin et al. 2008; Wang et al. 2010; Vijaya Lekshmi et al. 2011; Gulyaeva and Veselovsky 2012; Huba and Sazykin 2014). The former is the main approach to access the common features of ionospheric storms, especially for effects following numerous moderate geomagnetic storms, while the latter plays a significant role in understanding responses to the extreme storms in detail. Ionospheric parameters such as total electron content (TEC), stratified electron density, maximum electron density and height of F2 layers, as well as mean global electron content (GEC) (Chen et al. 2014), are used to describe and access the overall behavior of ionospheric responses to geomagnetic storms. The detailed discussion of ionospheric storm morphologies and mechanisms has been summarized by a series of excellent reviews (Buonsanto 1999; Mendillo 2006; Blagoveshchenskii 2013; Danilov 2013). It is believed that negative phases in high-latitude regions are related to decrease of O/N2 ratio and increased temperature. Negative phases propagate to middle-latitude regions with a speed of 50–300 m/s subsequently along with the equatorward wind (Jakowski et al. 1992; Mikhailov and Förster 1997). Usually, the more intense ionospheric negative effects are visible in summer hemisphere, due to the prevailing summer to winter thermospheric circulation (Fuller-Rowell et al. 1996). Nightside equatorward wind and the subsequent changes in neutral composition are accepted as the major causes leading to a more frequent occurrence of negative phases at midnight. In contrast, positive phases are the dominant ionospheric response to geomagnetic storms during the initial and main phase in the middle- and low-latitude regions (Wang et al. 2010). Comparing to the negative phases, the morphology and mechanisms of positive phases are more complicated. As summarized by Danilov (2013), E × B drift-induced F2-layers uplifting, plasma fluxes from plasmasphere and downwelling of gas are probable sources of ionospheric positive phase in middle- and low-latitude regions. The details of ionospheric storm morphologies and mechanisms dis-

cussion can be found in the review articles listed above and other references therein. In general, most of the typical features of ionospheric storms have been discussed in detail before the end of 1990s. Ionospheric storm morphologies are the combined effects of thermospheric circulation, Earth's electrodynamic and chemical changes. However, a systematic and comprehensive understanding of dramatic abnormal variations in different scales and complex nonlinear interaction among the thermosphere, ionosphere and magnetosphere during different storm phases of geomagnetic storms remain a challenge to be identified/to be understood (Mendillo 2006). The energy inputs to the ionosphere in space and time are not understood well now; namely, we do not know the relative importance of various processes as a function of position and time and their feedback effects. It is difficult to predict the ionospheric anomalous variation amplitude, duration and distribution accurately based on the solar wind conditions or geomagnetic indices in current stage. Case study of ionospheric storm will provide the detailed information, such as effects of the season, location and solar activity.

Fortunately, nowadays the global coverage, continuous and high temporal–spatial resolution GNSS ionospheric measurement provides abundant and high-quality Earth ionospheric observations (Hernández-Pajares et al. 2011; Jin et al. 2015). GPS TEC is widely used to reveal detailed temporal variations during different geomagnetic storm phases and global/local region features of ionospheric storm and provides us a new perspective to understanding the ionospheric response to geomagnetic storms (Lei et al. 2008, 2014; Zhao et al. 2009; Afraimovich et al. 2013; Galav et al. 2014). In spite of the numerous discussions published on ionospheric storms in the past decades, the ionospheric variations following the geomagnetic storms still cannot be modeled well and ionospheric storms are still the key to achieving an accurate TEC empirical forecast (Klimenko et al. 2012; Borries et al. 2015; Nava et al. 2016; Tulasi Ram et al. 2016). As we known, GPS TEC derived from regional or global ionospheric model has low precision (several TECU) while GPS TEC series from the GPS tracking arc contain the information of ionospheric horizontal gradient due to the moving ionospheric pierce points (IPP) (Zhao et al. 2016). With the quasi-invariant Geosynchronous Orbit (GEO) satellites of BeiDou Navigation Satellite System (BDS), the TEC series derived from BDS provide a new opportunity to catch the local details of ionospheric storm morphology by BDS GEO observations. In this paper, we aim to provide a detailed case study of ionospheric responses to the March 2015 storm, which is the most intense geomagnetic storms in solar cycle 24 up to now. Global ionospheric response and magnetic local time effects will be analyzed using global ionospheric maps provided by Center for Orbit Determination in Europe (CODE), while the BDS GEO ionospheric observation will

be used to explore the latitudinal differences of ionospheric storm effect. In addition, thermospheric composition changes derived from Global Ultraviolet Imager (GUVI) and Special Sensor Ultraviolet Spectrographic Imager (SSUCI) are utilized to discuss the possible mechanisms responsible for the observed TEC changes during the storm time.

2 Methods and data

Signal phase can be quantified by the integral of refraction index along the light of sight (LOS) between the transmitter and receiver in geometrical optics approximation. For signals propagating in Earth space, the high-order effects of ionospheric electron density and geomagnetic field are negligible at GNSS signal frequencies (L band). Then the frequency dependence ionospheric delay from multi-frequencies GNSS signals could be used to derive TEC along the LOS as equation 1 (Jin et al. 2008 and Jin et al. 2016)

$$
\begin{aligned}
\text{STEC} &= \frac{f_1^2 f_2^2}{40.3(f_1^2 - f_2^2)}(L_1 - L_2 - (\lambda_1 N_1 - \lambda_2 N_2) \\
&\quad - (d_{r1} - d_{r2} + d^s{}_1 - d^s{}_2) + \varepsilon_{L12}) \\
&= \frac{f_1^2 f_2^2}{40.3(f_2^2 - f_1^2)}(P_1 - P_2 - (d_{r1} - d_{r2} \\
&\quad + d^s{}_1 - d^s{}_2) + \varepsilon_{P12})
\end{aligned}
\tag{1}
$$

where f is carrier phase frequency; L, P are GNSS carrier phase and pseudorange observations; d is instrument biases of corresponding receivers and satellites; λ is wavelength of carrier phase; N is carrier phase integer ambiguity; and ε is multipath effect and other unmodeling residuals. With continuous observation provided by worldwide GNSS stations, the temporal–spatial variations of Earth's ionosphere in TEC series could be detected. Since the end of 2012, the BeiDou navigation system tri-frequency signal has become available for the public. A number of BDS continuous operating BDS tracking stations were subsequently built up, such as Beidou Experimental Tracking Stations (BETS) and Multi-GNSS Experiment (MGEX) (Jin et al. 2016). Unlike other GNSS constellation, BDS constellation consists of five GEO, five IGSO (inclined geosynchronization orbit) and four MEO (medium Earth orbit) satellites on orbits up to now (http://www.beidou.gov.cn). With the benefit of GEO quasi-invariant orbital locations, TEC series derived from GEO measurement are less dependent on the ionospheric spatial gradient induced by ionospheric pierce points' movement that would be mixed in non-geosynchronous Earth orbit satellites ionospheric observations. Unlike ionospheric variation detection with global ionospheric maps (GIMs), BDS GEO TEC could be extracted from the frequency difference of carrier phase after carrier phase leveling and instrument biases calibration without modeling error from spherical harmonic

expansion or temporal–spatial interpolation. Furthermore, the interval of BDS GEO TEC is equal to the sampling rate of BDS observations which can show us more details of ionospheric storms.

It is well known that ionospheric variation consists of periodic background variation and disturbances triggered by human activities and natural events such as rocket launchings, earthquakes and geomagnetic storms (Richards 2001; Tsai et al. 2001; Ding et al. 2014; Jin et al. 2014; Mangla et al. 2014). As summarized by Mendillo (2006), the duration of geomagnetic storm-induced ionospheric disturbance could last up to several days. We choose the mean values of corresponding epochs in the 10 days with quietest geomagnetic conditions in March 2015 as the TEC references. The TEC is stable in the same epoch and location without specific events. Here we define the part of out of two times standard deviation threshold as the quantity of ionospheric anomaly. As described in Eq. 2, if TEC is less than the lower boundary, the ionospheric storm should present a negative phase; on the contrary, it shows positive phase.

$$
\text{dTEC} = \begin{cases} \text{TEC}_t - (\text{mean}(\text{TEC}_{q,t}) + 2\text{std}(\text{TEC}_{q,t})), \text{positive} \\ \text{TEC}_t - (\text{mean}(\text{TEC}_{q,t}) - 2\text{std}(\text{TEC}_{q,t})), \text{negative} \end{cases}
\tag{2}
$$

BDS GEO ionospheric observations from eighteen BDS stations distributed at $0°\text{E} - 165°\text{W}$ (geodetic longitude) as shown in Fig. 1 provided by Multi-GNSS Experiment (MGEX) are used to demonstrate the detailed local effect following the intense ionospheric storms. Here only observations with satellite elevation angles greater than 15 degrees are considered in order to avoid large mapping function errors. On the other hand, GIMs released by ionospheric-related scientific communities such as CODE, ESA, UPC and JPL since the end of last century have become a valuable source of information for ionospheric study (Hernández-Pajares et al. 2009). Here, one hour interval of GIM with 2.5×5 degree spatial resolution released by CODE (ftp://cddis.nasa.gov/pub/gps/products/ionex/) is used to analyze and discuss the global ionospheric response to the March 2015 storm.

3 Observational results

3.1 Geophysical condition of the March 2015 storm

Although solar cycle 24 is likely the weakest cycle since 1932, as suggested by the observed and prediction sunspot number series, and the level of geomagnetic activity was low during the rise phase of this cycle (Richardson 2013), a strong geomagnetic storm occurred on March 17, 2015. Figure 2 presents the variations of the geomagnetic indices and F10.7 solar flux proxy in March 2015. Figure 2a shows meridional

Fig. 1 Distribution of BDS GEO observations. The *red circles* are locations of BDS stations; *triangles* show projections of BDS GEO on the ground; crosses are ionospheric pierce points (IPPs) at 450 km altitude assumed central ionospheric shell (only mark GEO IPPs with satellite elevation larger than 15°)
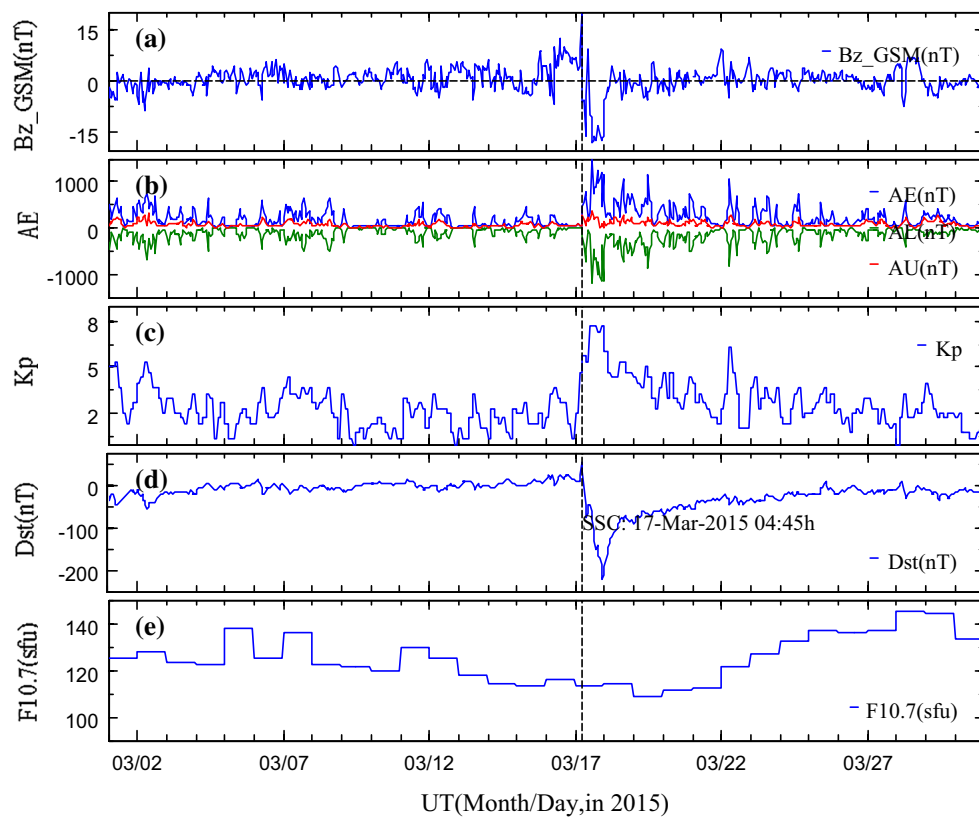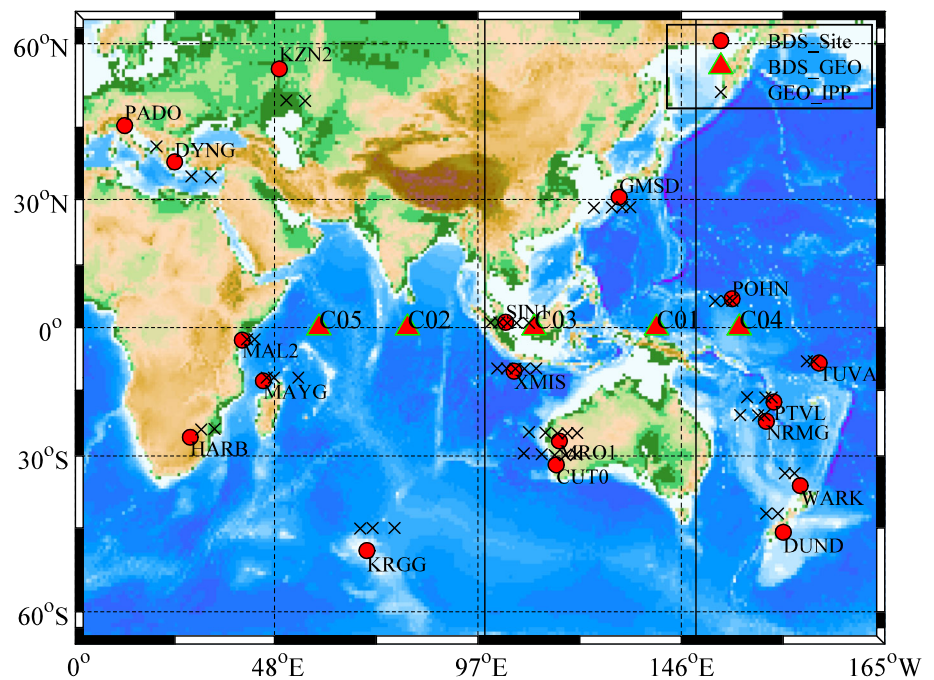
Fig. 2 Geomagnetic indices and F10.7 solar flux variations in March 2015. The *vertical dashed line* shows the epoch of storm sudden commence (SSC)

component of solar wind-induced interplanetary magnetic field (IMF) in Geocentric Solar Magnetospheric (GSM) coordinate system, i.e., Bz_GSM, observed by Advanced

Composition Explorer (ACE). It is generally accepted that long time (more than 3 hour) southward IMF (Bz_GSM < 0) is an indicator of the occurrence and development of one

geomagnetic storm (Liu and Li 2002; Gonzalez and Echer 2005). As shown in Fig. 2a, Bz_GSM decreased dramatically at 04:45 UT on March 17 and it reached to a minimum of -17.5 nT. Moreover, Bz_GSM kept southward for more than one day. Energy, mass and momentum from solar wind flow are transferred to Earth's magnetosphere following the merging and reconnection between IMF and Earth's magnetic field. Figure 2b presents Auroral Electrojet (AE) indices in March 2015. An enhancement in westward Auroral Electrojet recorded by AL index series dominated AE index disturbance occurs following the Bz_GZM southward turning. Rapid geomagnetic responses to the solar wind disturbance are also shown in middle- and low-latitude regions detected by Kp index and Dst variation. As shown in Fig. 2c, d, Kp index reached up to 8 during the main phase, while the Dst reached -223 nT at 22 UT on March 17. It should be mentioned that solar flux proxy F10.7 was relatively stable during this period (Fig. 2e). Although the interplanetary magnetic field and Auroral Electrojet recovered to pre-quiet level rapidly as shown Fig. 2a, b, the Earth magnetic field remained anomalous until March 25 as shown in Kp index and Dst series. Here the quiet period geomagnetic activity level is determined by the corresponding indices on the international ten quietest days in March 2015 (http://wdc.kugi.kyoto-u.ac.jp). Our discussion in the following section will focus on the time window of March 15 to 26 in 2015. With symmetrical disturbance field in H series, i.e., SYM-H that is essentially the same as hourly Dst index, three phases (initial phase, main phase and recovery phase) of this geomagnetic storm are defined as 04:45 UT (Storm Sudden Commencement, SSC) to 06:22 UT on March 17, 2015, 06:22 UT on March 17 to 22:47 UT on March 17 main phase and 22:47 UT on March 17 to 10:02 UT on March 25 recovery phase.

3.2 Local ionospheric disturbance from BDS GEO TEC

With dual-frequency GEO observations provided by eighteen BDS continuous operating stations as shown in Fig. 1, high temporal resolution TEC variations without satellite movement effects are obtained during March 2015. As an example, BDS GEO TEC series from the station CUT0 are presented in Fig. 3. The five IPPs are almost at the same geomagnetic latitudes, while the geomagnetic longitudes vary from 167°W to 178°W and the elevation angles vary between 19.2° and 52.3°. The TEC variation is almost the same for the five BDS GEO observations. Clear TEC enhancements are observed during the main phase and then TEC depletion is seen during the storm recovery phases from all of the five GEO satellites' observations, although their IPP locations could be more than one thousand kilometer apart in zonal direction and their elevation angles are also different. Therefore, we chose only one GEO TEC series with highest satellite elevation angle to analyze characteristics of the ionospheric storm.
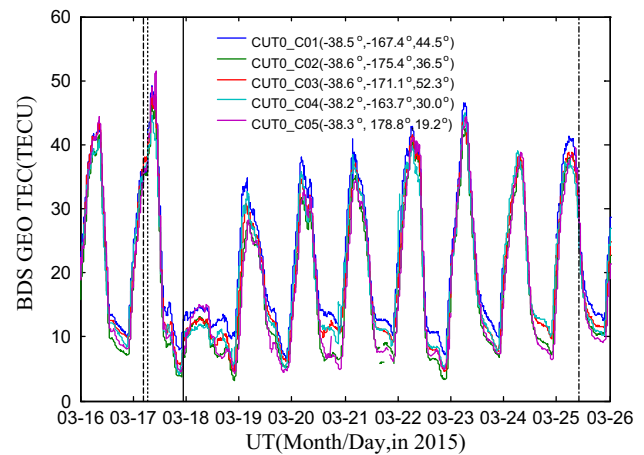

Fig. 3 BDS GEO TEC observations from MGEX station CUT0. Three angles in the brackets are IPPs' geomagnetic latitudes, longitudes and satellite elevation angles at receivers of corresponding BDS station and satellite pairs. The *vertical dashed*, *dotted*, *solid* and *dash dot lines mark* the epoch of storm sudden commence (SSC), the beginning of Dst decrease, Dst peak value (i.e., end of main phase) and end of recovery phase. IPPs geomagnetic latitudes, longitudes, satellite elevation angles and geomagnetic phase separator are marked in the same way in the following figures

Using the method introduced in Sect. 2, ionospheric disturbances derived from the eighteen BDS stations' GEO observation are presented in Figs. 4, 5 and 6. The ionospheric disturbance series in nightside (solar zenith > 90°) are marked with gray rectangular patches, respectively. Figure 4 presents BDS GEO TEC observations in European region (0°E − 70°E). The SSC epoch is around local dawn, while the peak Dst epoch is around the midnight in this region. During the main phase, clear positive phases are detected by measurement obtained from stations located in middle- to high-latitude regions and develop to the maximum near local noon, while the positive phase around noon are not visible in BDS GEO TEC series in lower latitudes (MAL2_C05 and MAYG_C05). The second prominent positive phase appears in TEC series provided by PADO_C05, DYNG_C05 and HARB_C05 around post-dusk. Unlike the first dayside positive phase, the second post-dusk positive phase only appears in middle latitudes. Morphology of this ionospheric storm is different during the recovery phase. Negative phases appear repeatedly in dayside from March 18 to 22 as illustrated in Fig. 4. It is necessary to point out that negative phases will last to post-midnight in low-latitude regions as shown in TEC series provided by MAL2_C05 and MAYG_C05.

Figure 5 shows the ionospheric storm variation in the Asia–Australia region (70°E–140°E). The main phase of the storm mainly falls into the nightside sector. Almost no positive phases are observed in this region during main phase, except KRGG_C02. Positive phase is visible during the daytime in TEC series provided by high-latitude-located BDS

Fig. 4 Negative phase and positive phase from observation provided by BDS stations located in European region (0°E–70°E). The *blue lines* are the observed *vertical* TEC series; the *green lines* are the quiet time background TEC variation; the *red lines* are negative and positive phases defined in Sect. 2. Nighttime periods are marked with *gray rectangular* patches
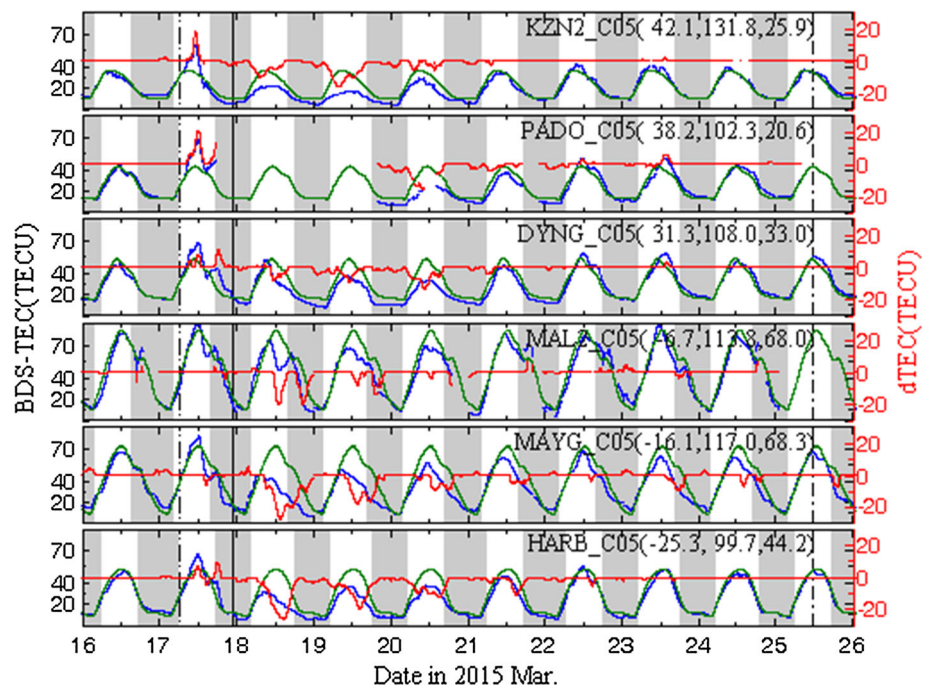
Fig. 5 Negative phase and positive phase from observation provided by BDS stations located in Asia–Australia region (70°E–140°E)
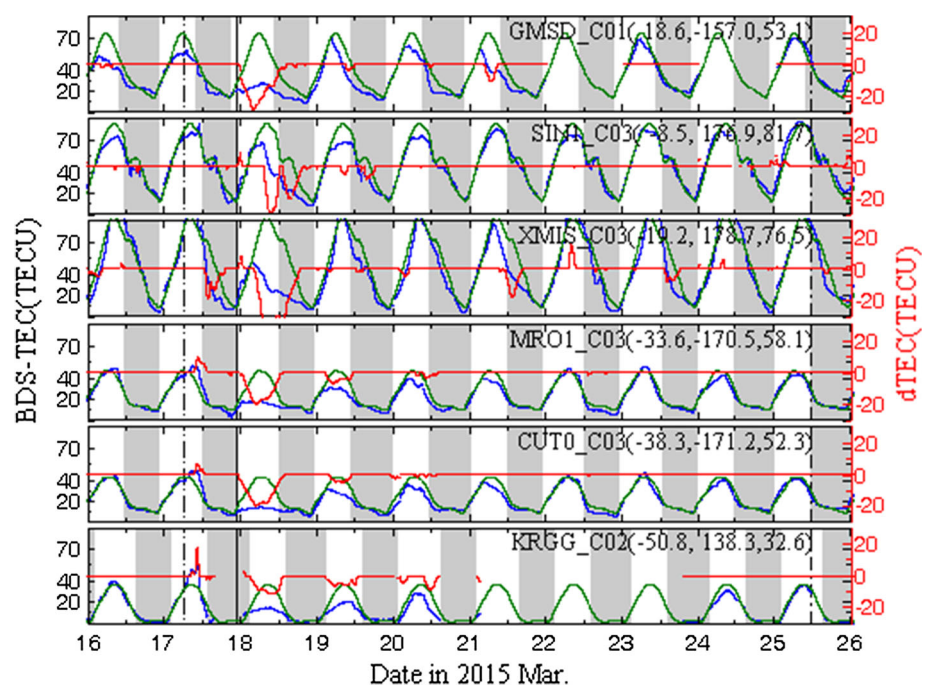
station KRGG that is similar to ionospheric storm in European region. Similar to European region, negative phases are still dominated during the recovery phase in this sector, and they mainly appear in dayside sector not only for the low-latitude regions but also the middle- and high-latitude regions (KRGG_C02) in south hemisphere. The bigger negative phases in nightside are also detected in low-latitude BDS GEO TEC observations in this region (SIN1-C03, XMIS_C03), which are probably due to the high [O]/[N2]

ratio and large equatorial electrojet (EEJ) (see discussion below). An isolated short-duration disturbance is detected with GMSD on March 22 that maybe related to the submagnetic disturbance remarked by AE and Dst indices.

Figure 6 presents the ionospheric disturbance in the western Pacific region. The six stations in Fig. 6 are not far away from stations shown in Fig. 5, and the morphology of ionospheric storm in this area is similar to Asia–Australia region for corresponding latitudes and local time sectors.
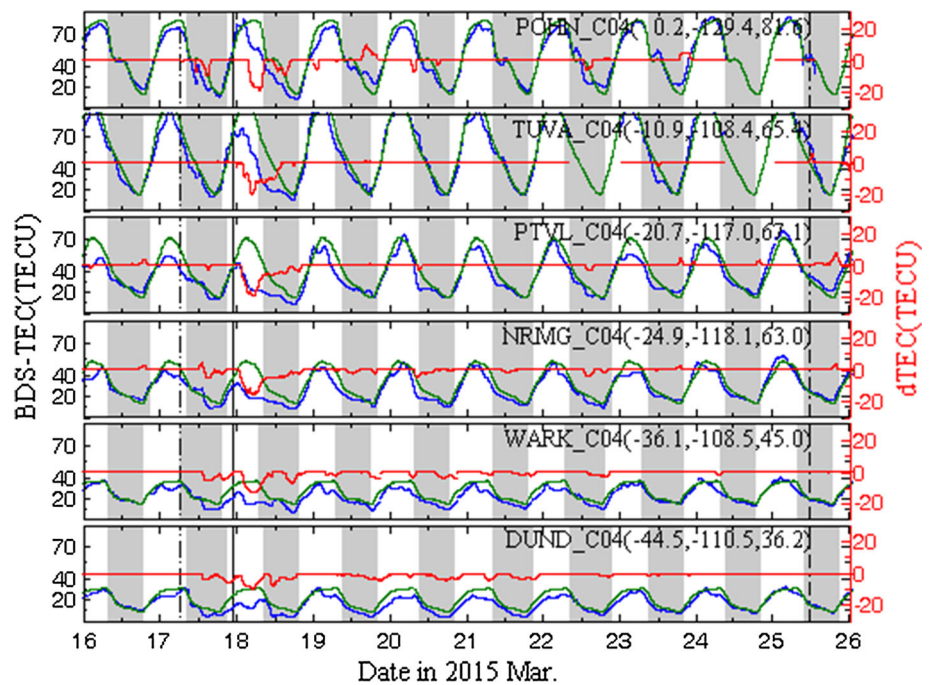
Almost no positive phases are detected in this sector, while negative phases are visible in TEC series from southern hemispheric low-/middle-latitude-located stations CKIS, TONG and NRMG in the post-midnight sector during main phase. Negative phases during the recovery phase show a similar pattern to the two other regions. However, the amplitudes seem to depend on local conditions. For example, the major negative phases in XMIS-C03 and PTVL-C04 TEC series appear at similar local time sectors, while the amplitude has large difference although the IPPs are both located around S20°.

In general, prominent ionospheric disturbances present different morphologies during the main phase and recovery phase in different latitudes and local time sectors. During main phase, amplitude of positive phases are up to dozens of TECUs recorded by BDS stations located at high-to-middle latitudes, while almost no positive phase is detected at nightside in high latitudes and the subsequent post-dusk positive phases are detected at middle latitudes. At low-latitude regions, nightside ionospheric negative phase is the dominant response to the geomagnetic storm. Morphology of this ionospheric storm is different during the recovery phase as compared with that during the main phase. Dayside negative phases prevail during 18–22 March at almost all the latitudes and their amplitudes decrease gradually as the storm recover back to quiet level. Besides, pronounced post-dusk negative phase is another important feature of low-latitude ionospheric storm morphology.

Statistics of dayside and nightside ionospheric disturbance peaks is given in Tables 1 and 2. Positive phases reached the peak around 10–12 UT on March 17 in the local afternoon sectors. Around 17–18 UT on March 17, a second positive phase peak appears in the post-dusk sectors in lower-latitude regions (Table 1). The peaks have smaller amplitudes and appear later (except NRMG_C04) in lower-latitude regions for both positive phase peaks in the dayside and nightside. Table 2 presents the UT, magnetic local time and amplitude of dayside and nightside negative phase peaks. The first negative phase peak appears in dayside around 04–15 UT on March 18 at the beginning of the storm's recovery phase, and the second negative phase peak appears around 13–20 UT in nightside on March 18. Unlike the first dayside negative phases, the nightside ones are mainly distributed in low latitudes. No obvious UT dependency for the appearance of negative peaks in different geomagnetic latitudes is detected by the eighteen BDS GEO TEC observations, and it is clear that the most intense negative phase is formed in lower-latitude regions that is opposite from the situation of positive phase. Higher background TEC value may be one of the contributors for the higher negative phase peaks in low-latitude regions. Besides the latitudinal dependence, the global evolution of ionospheric storms also depends on local times (Prölss 1995).

3.3 Global morphology of ionospheric storm variations

Although the ionospheric response to the geomagnetic storm could be seen in detail with high temporal and high precision BDS GEO TEC series, it is difficult to picture the ionospheric storm morphology in global scale with the limit of available BDS continuous stations and sparse IPPs distribution up to now. GIMs with one hour interval released by CODE are used

Table 1 Statistics of dayside and nightside positive phase peaks

	MLat.	Dayside PP			Nightside PP		
		Day, UT	MLT	Maximum σ TEC	Day, UT	MLT	Maximum σ TEC
KRGG_C02	−50.8	17 10:18	14.6	18.3			
CUT0_C03	−38.3	17 10:23	18.0	6.2	17 11:41	19.3	3.0
MRO1_C03	−33.6				17 10:36	18.3	9.3
HARB_C05	−25.3	17 11:57	13.6	7.9	17 17:47	19.5	9.3
NRMG_C04	−24.9				17 13:03	0.2	3.9
TUVA_C04	−10.9				17 18:03	5.8	1.1
MAL2_C05	−6.7				17 17:02	19.6	2.8
DYNG_C05	31.3	17 11:56	14.2	7.4	17 18:18	20.5	10.7
PADO_C05	38.2	17 12:03	13.9	20.4			
KZN2_C05	42.1	17 11:06	14.9	17.6			

Table 2 Statistics of dayside and nightside negative phases

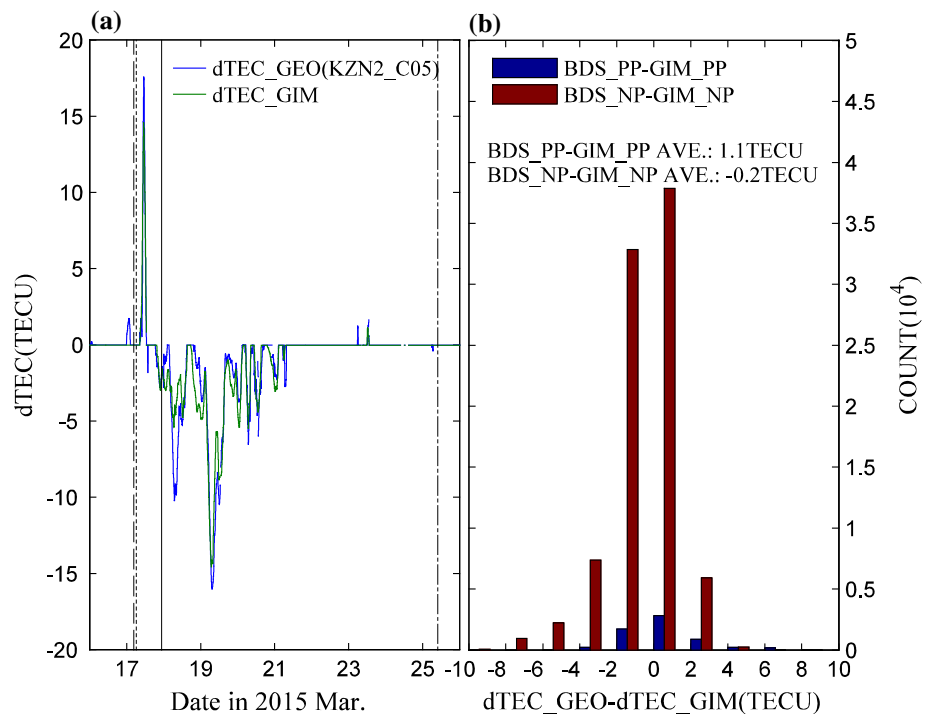|		Dayside NP			Nightside NP		
		Day, UT	MLT	Minimum σ TEC	Day, UT	MLT	Minimum σ TEC
KRGG_C02	−50.8	18 09:49	14.1	−11.0			
DUND_C04	−44.5	18 04:52	16.5	−9.2			
WARK_C04	−36.1	18 05:20	17.1	−12.8			
CUT0_C03	−38.3	18 04:47	12.4	−19.5			
MRO1_C03	−33.6	18 04:47	12.4	−19.8			
HARB_C05	−25.3	18 14:39	16.3	−25.2			
NRMG_C04	−24.9	18 05:20	16.5	−15.9			
PTVL_C04	−20.7	18 04:43	15.9	−19.4			
MAYG_C05	−16.1	18 13:33	16.4	−27.8	18 17:18	20.1	−20.2
XMIS_C03	−19.2	18 08:43	15.7	−49.7	18 13:00	19.9	−33.8
TUVA_C04	−10.9	18 04:43	16.5	−19.6	18 08:23	20.2	−12.7
MAL2_C05	−6.7	18 12:46	15.4	−20.2	18 20:30	23.1	−19.6
SIN1_C03	−8.5	18 09:30	16.3	−28.6	18 15:55	22.7	−20.4
POHN_C04	0.2	18 07:07	17.5	−19.1	18 15:02	1.4	−9.7
GMSD_C01	18.6	18 04:08	12.7	−28.5			
DYNG_C05	31.3	18 11:22	13.6	−8.6			
KZN2_C05	42.1	18 07:00	10.8	−10.2			

to show global ionospheric response to the March 2015 geomagnetic storm. Figure 7 presents the difference between GIMs interpolated TEC derived disturbance and the result from KZN2_C05 observations. The ionospheric disturbances from GIMs and BDS GEO TEC basically agree with each other. The large-scale features of severe ionospheric disturbances detected by BDS GEO observations are also detected by GIMs interpolated TEC series, although the later has lower amplitudes for the three main peaks. The right panel of this figure shows the differences of positive phase observed from eighteen BDS GEO stations and the corresponding GIM TEC changes during the geomagnetic storm. In most case, the TEC differences fall into ±2 TECU that is within the root mean

square (RMS) of CODE GIMs. The average of positive and negative phase differences are 1.1 TECU and 0.2 TECU that is much smaller than the scale of TEC disturbance following the geomagnetic storm discussed above. It is reasonable to use GIMs to analyze ionospheric storm in March 2015 in global scale although GIMs have higher RMS and lower temporal resolution.

Figure 8 presents the evolutions of ionospheric TEC disturbances at the fixed Magnetic Local Time (MLT) frames during the March 2015 storm. It is clear that negative phases persist till to the end of recovery phase in high- and middle-latitude regions and their amplitude decrease as the Dst recover to the quiet level at both dayside and nightside, while

Fig. 7 Ionospheric disturbance from KZN2_C05 observations and GIM interpolated TEC series at corresponding IPP location (*left*). The distribution of negative (*red*) and positive (*blue*) phase amplitude difference from eighteen BDS GEO TECs presented in Fig. 4 and corresponding GIM interpolated TECs (*right*)

the most pronounced negative phases appear at lower latitudes. The TEC changes are generally quasi-symmetrical in two hemispheres, since this storm occurred in equinox. Compared with the nightside, dayside negative phase has larger amplitude, longer duration and wider latitude range. Unlike major negative phase, positive phases tend to have shorter duration and confined region. During the main phases, positive phases are mainly pronounced at middle-latitude regions in daysides and post-dusk sectors for both hemispheres. Note that the positive phase in the southern hemisphere has a time delay corresponding to the northern hemisphere. In the recovery phase, pronounced positive phases mainly appear during the morning sector in low-latitude regions on March 18.

3.4 MLT dependence of the TEC disturbance

In order to further investigate the MLT dependence of ionospheric storm effect in a qualitative way, the negative and positive phase peaks geomagnetic latitudes and amplitudes in different MLT sectors are presented in Fig. 9. The peak amplitudes and the corresponding geomagnetic latitudes of negative phase and positive phase show quasi-north–south symmetry in MLT sectors during the main phase and the first day of recovery phase, while the situation of negative and positive phase shows large differences. During the main phase, amplitudes of positive phase peaks are up to 40 TECU in the afternoon sector (around 16–18 MLT) and around 10 TEU in other MLT sectors, while NP amplitude is around 10 TECU in all MLT sectors in two hemispheres. The maximum negative phase appears at higher geomagnetic latitudes except around

midnight (MLT 22–04) when it appears in lower geomagnetic latitude regions compared to the positive phase. During the recovery phase, the negative phase amplitude reaches to the peak (around 40–50 TECU) in the afternoon sector at around 16 MLT, and negative phase reaches its peak (30–60 TECU) around MLT=20. Except for post-midnight sectors, ionospheric disturbances with maximum amplitudes always appear in low-latitude regions (lower than 30°). During the post-midnight sectors, maximum negative phases appear in mid-high latitudes. Negative ionospheric phase becomes the dominant feature during the storm recovery phase.

4 Discussion

The ionospheric anomalies during the March 2015 geomagnetic storm are up to about 30 TECU, corresponding to about 4.8 meters delay in BDS L2/L6 frequency observations (e.g., Fig. 4), which have great effects on GNSS navigation, positioning and geodesy applications at centimeter accuracy. Therefore, such ionospheric delay must be corrected using BDS ionospheric delay estimation or dual-frequency ionospheric-free combination. In addition, the understanding of such ionospheric disturbances will contribute to know the sources and establish better empirical models. It is well known that thermospheric variation, as one of the important processes near Earth's space, can significantly modify the state of Earth's ionosphere. The column density of atomic oxygen ([O]) and molecular nitrogen ($[N_2]$) ratio, i.e., $[O]/[N_2]$ ratio, has been used as an indicator of thermo-

dTEC(TECU)
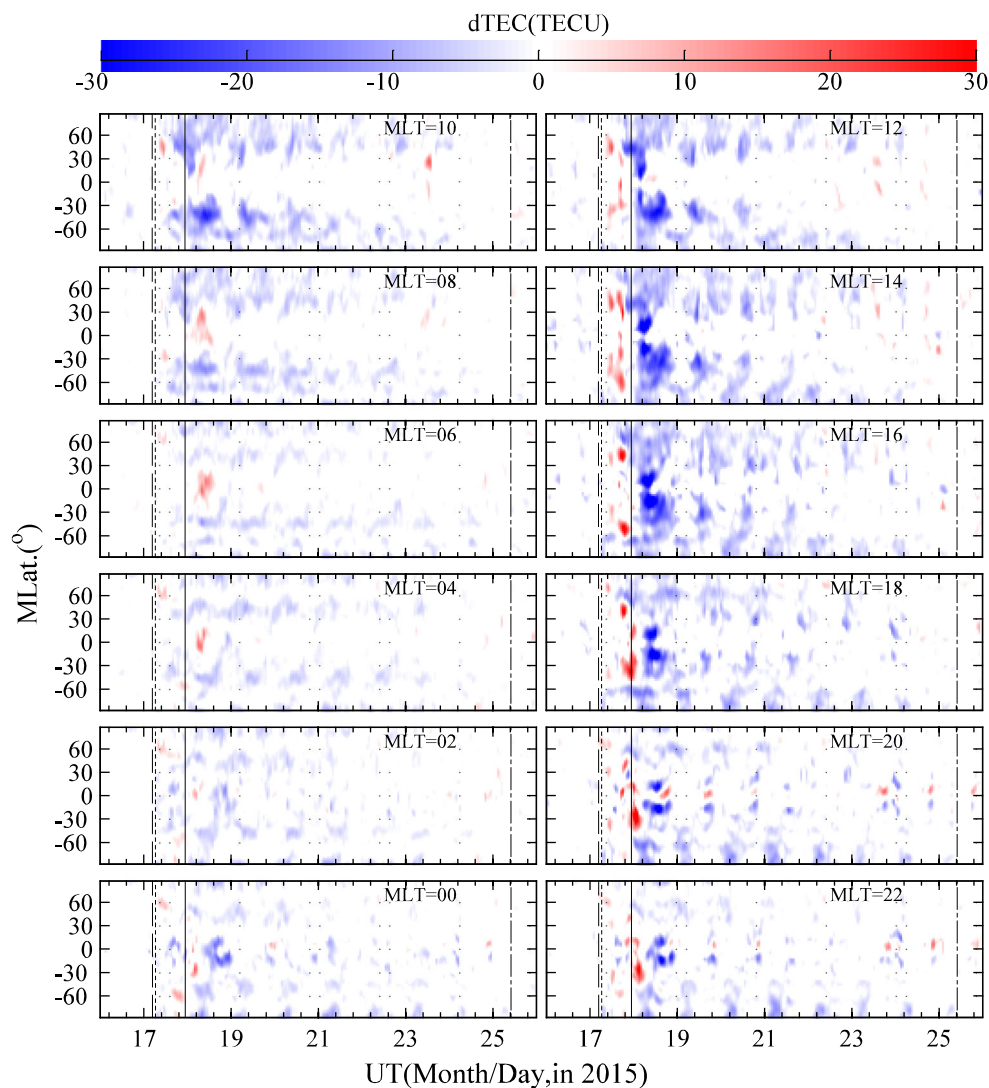
Fig. 8 Time variation of ionospheric disturbances derived from GIMs in different MLT sectors during March 16–26 in 2015

spheric composition change in geomagnetic effects analysis (Zhang et al. 2004; Kil et al. 2011). During the storm in March 2015, OI emission and N_2 Lyman–Birge–Hopfield (LBH) dayglow measurement are available from Global Ultraviolet Imager (GUVI) onboard Thermosphere, Ionosphere, Mesosphere Energetics and Dynamics (TIMED) spacecraft (http://guvi.jhuapl.edu/) and Special Sensor Ultraviolet Spectrographic Imager (SSUSI) onboard Defense Meteorological Satellite Program(DMSP) spacecrafts F16, F17 and F18 (http://ssusi.jhuapl.edu/). The derived $[O]/[N_2]$ ratio variation from 16 March to 26 March from data collected by sensors on these four spacecrafts is presented in Fig. 10. All of these four spacecrafts fly in sun-synchronous orbits at thermospheric height that provides us an opportunity to study evolution of thermospheric response in different MLT sectors.

Significant $[O]/[N_2]$ ratio reduction in high-latitude regions are detected by SSUSI_F16, SSUSI_F18 and GUVI_TIMED around the peak Dst epoch. The depletion tends to develop into lower-latitude zone that agrees well with the negative ionospheric storm morphology. Furthermore, the $[O]/[N_2]$ ratio reduction repeats on the following days especially for MLT = 8–10 (Fig. 10b, d). This thermospheric composition variation should be an important source of the dayside repeated negative phase in high-to-middle latitudes during the recovery phase. As we known, thermospheric composition changes should not be the major contribution to the ionospheric positive phase observed during the main phase when no obvious variation is seen in $[O]/[N_2]$. Nevertheless, during the late of the main phase and the recovery phase period, $[O]/[N_2]$ ratios increased at low and middle latitudes around MLT16 and MLT08 sectors as shown in Fig. 10a, d. Subsequently, positive ionospheric phases are
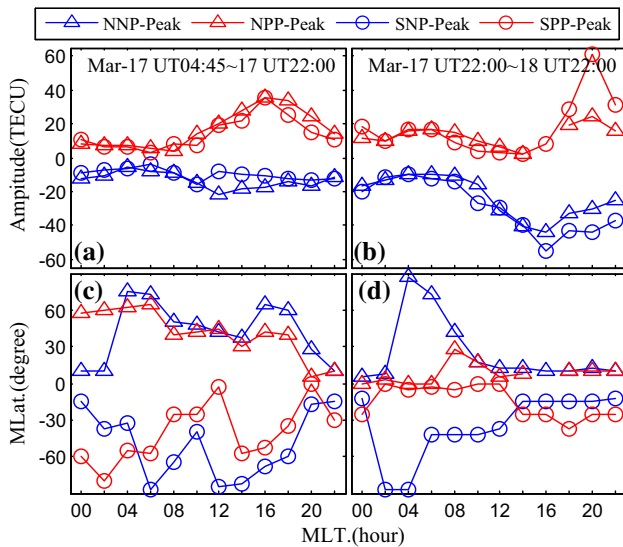
Fig. 9 Amplitude (peak value) and corresponding geomagnetic latitude of negative phase and positive phase in north/south hemispheres during main phase and the first day of recovery phase in different MLT sectors. Here the negative phase (NP) and positive phase (PP) are represented in *blue* and *red color*. North hemispheric NP (NNP) and North hemispheric PP (NPP) are by *triangles*, South hemispheric NP (SNP) and South hemispheric PP (SPP) are marked by *circles*

detected in low latitude as shown in Fig. 8. Neutral composition might play an important role in producing positive ionospheric phase during this period.

Besides neutral composition, electric fields and neutral winds also play an important role in determining the strength of the storm effect, especially during the initial and main phases (Lei et al. 2008; Wang et al. 2010). In order to examine the possible contribution of the electric field to the observed storm effect on March 17, 2015, the vertical plasma drift is investigated. Unfortunately, the C/NOFS (Communication/Navigation Outage Forecasting System) satellite data are not available in 2015. Yue et al. (2016) carried out the simulations from the thermosphere ionosphere electrodynamics general circulation model (TIEGCM) and showed similar large-scale ionospheric disturbances, indicating that the neutral wind and the E × B drift disturbance might be responsible for the storm effect. During the daytime, the weaker E × B tends to move the ionosphere to lower altitudes and therefore will cause positive storm effect. The downward E × B drift disturbance results a negative storm effect. In addition, the prompt penetration electric fields (PPEF) could be the possible physical mechanisms on the ionospheric response to the storm-induced disturbances (Huang
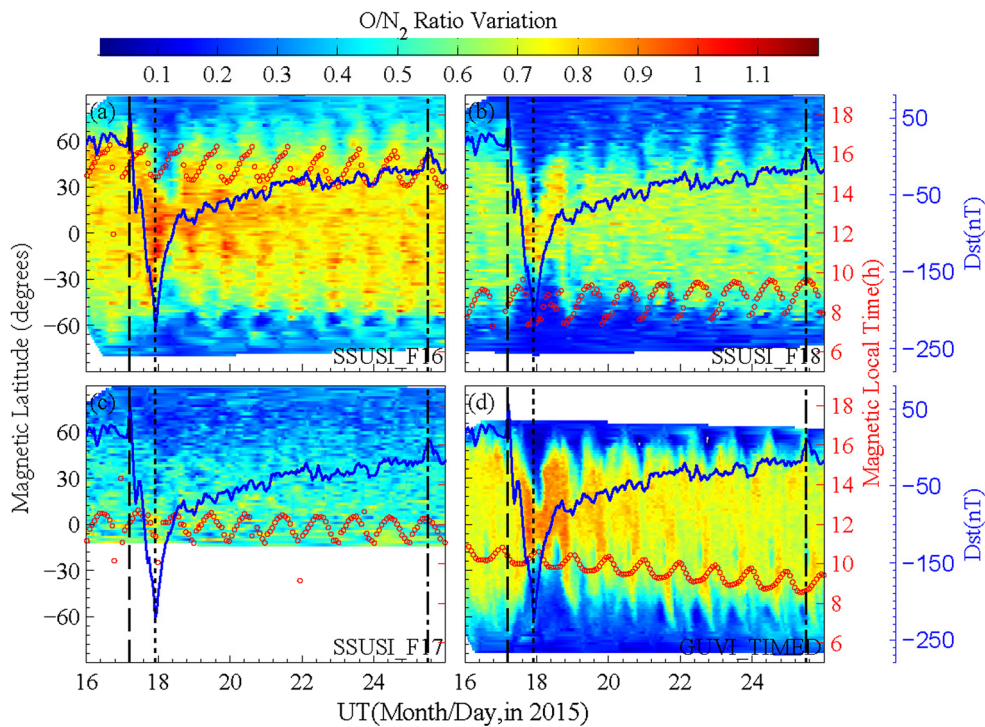
Fig. 10 [O]/[N$_2$] ratio variation during the geomagnetic storm in March 2015 observed by GUVI and SSUSI. In order to show thermospheric response to magnetic storms, Dst series represented with the blue line is superimposed on the [O]/[N2] ratio maps. The *red circle* is the MLT mean values for one single orbit. The three *vertical black lines* are similar to the lines in Fig. 3

et al. 2005). The European Space Agency (ESA)'s mission SWARM was successfully launched on November 22, 2013, with three identical satellites at polar orbits with inclinations of $87-88°$, which can investigate the dynamics of the Earth's magnetic field as well as the ionospheric and thermospheric environment. The equatorial electrojet results obtained from the magnetic SWARM data showed that the storm-time penetration electric fields are most probably the main driver of the observed ionospheric responses to this storm (Astafyeva et al. 2016). Therefore, the observed positive and negative storms are mainly associated with the changes of the disturbance dynamo electric fields and prompt penetration electric fields.

5 Summary

The morphology of ionospheric response to the March 2015 strong geomagnetic storm was investigated on the basis of BDS GEO observations and GIM TEC maps. Local and global negative and positive ionospheric response to the intense geomagnetic storm is presented in detail. During the main phase, ionospheric positive storm is the dominant feature, while negative phases are the dominant response to the geomagnetic storm that continue to be visible in high- and middle-latitude regions till to March 23 in recovery phase. Although the spatial distribution of available BDS GEO observations is limit now, local ionospheric disturbances such as positive phase in dayside and the followed positive phase in nightside, recurrence negative phase in afternoon sector and difference of anomalies amplitudes are detected by BDS GEO TEC that is free from the movement of satellite and modeling error of harmonic spherical expanding. On the other side, reconstructed GIMs interpolated TEC give us a full picture of the ionospheric storm in large scale. Although GIMs have low temporal–spatial resolution, the interpolated TEC could provide the ionospheric disturbance in general except lower amplitude for some large peaks when compared to BDS GEO observations. Ionospheric responses to the storm in different MLT sectors are discussed in detail. Dual-peak (one is in dayside and the other is in nightside) positive phase and repeated negative phase in dayside are detected by BDS GEO data. Although the positive phase is dominant in the main phase and the negative phase mainly appears in the recovery phase, both the maximum negative and positive phases appear in the afternoon and post-dusk sectors in main and recovery phase of the geomagnetic storm. The latitudinal dependence of the ionospheric storm effects varies with the storm phase, although it presents quasi-symmetrical in the south and north hemispheres. Positive phases mainly appear in the main phase near the noon and the first days of recovery phase around the dusk with shorter duration and

smaller area. Thermospheric composition variations play an important role in the development of ionospheric storm in March 2015 seen by [O]/[N2] ratio data as well as disturbance dynamo electric fields and prompt penetration electric fields.

References

Afraimovich EL, Astafyeva EI, Demyanov VV et al (2013) A review of GPS/GLONASS studies of the ionospheric response to natural and anthropogenic processes and phenomena. J Space Weather Space Clim 3:A27. doi:10.1051/swsc/2013049

Astafyeva E, Zakharenkova I, Alken P (2016) Prompt penetration electric fields and the extreme topside ionospheric response to the June 22–23, 2015 geomagnetic storm as seen by the Swarm constellation, Earth. Planets Space 68:152. doi:10.1186/s40623-016-0526-x

Borries C, Berdermann J, Jakowski N, Wilken V (2015) Ionospheric storms: a challenge for empirical forecast of the total electron content. J Geophys Res: Space Phys 120(4):3175–3186. doi:10.1002/2015JA020988

Blagoveshchenskii DV (2013) Effect of geomagnetic storms (substorms) on the ionosphere: 1. A review. Geomagn Aeron 53(3):275–290. doi:10.1134/S0016793213030031

Buonsanto MJ (1999) Ionospheric storms: a review. Space Sci Rev 88(3):563–601. doi:10.1023/A:1005107532631

Chen Y, Liu L, Le H, Wan W (2014) Geomagnetic activity effect on the global ionosphere during the 2007–2009 deep solar minimum. J Geophys Res: Space Phys 119(5):3747–3754. doi:10.1002/2013JA019692

Danilov AD (2013) Ionospheric F-region response to geomagnetic disturbances. Adv Space Res 52(3):343–366. doi:10.1016/j.asr.2013.04.019

Ding F, Wan W, Liu L, Afraimovich EL, Voeykov SV, Perevalova NP (2008) A statistical study of large-scale traveling ionospheric disturbances observed by GPS TEC during major magnetic storms over the years 2003–2005. J Geophys Res: Space Phys 113:A00A01. doi:10.1029/2008JA013037

Ding F, Wan WX, Mao T, Wang M, Ning BQ, Zhao BQ, Xiong B (2014) Ionospheric response to the shock and acoustic waves excited by the launch of the Shenzhou 10 spacecraft. Geophys Res Lett 41(10):3351–3358. doi:10.1002/2014GL060107

Echer E, Gonzalez WD, Tsurutani BT (2011) Statistical studies of geomagnetic storms with peak Dst ≤ -50 nT from 1957 to 2008. J Atmos Solar Terr Phys 73(11):1454–1459. doi:10.1016/j.jastp.2011.04.021

Fuller-Rowell TJ, Codrescu MV, Rishbeth H, Moffett RJ, Quegan S (1996) On the seasonal response of the thermosphere and ionosphere to geomagnetic storms. J Geophys Res: Space Phys 101(A2):2343–2353. doi:10.1029/95JA01614

Galav P, Rao SS, Sharma S, Gordiyenko G, Pandey R (2014) Ionospheric response to the geomagnetic storm of 15 May 2005 over midlatitudes in the day and night sectors simultaneously.

J Geophys Res: Space Phys 119(6):5020–5031. doi:10.1002/2013JA019679

Gonzalez WD, Echer E (2005) A study on the peak Dst and peak negative Bz relationship during intense geomagnetic storms. Geophys Res Lett. doi:10.1029/2005GL023486

Gulyaeva TL, Veselovsky IS (2012) Two-phase storm profile of global electron content in the ionosphere and plasmasphere of the Earth. J Geophys Res: Space Phys 117:A09324. doi:10.1029/2012JA018017

Hernández-Pajares M, Juan JM, Sanz J, Orus R, Garcia-Rigo A, Feltens J, Komjathy A, Schaer SC, Krankowski A (2009) The IGS VTEC maps: a reliable source of ionospheric information since 1998. J Geod 83(3–4):263–275. doi:10.1007/s00190-008-0266-1

Hernández-Pajares M, Juan JM, Sanz J, Aragón-Àngel À, García-Rigo A, Salazar D, Escudero M (2011) The ionosphere: effects, GPS modeling and the benefits for space geodetic techniques. J Geod 85(12):887–907. doi:10.1007/s00190-011-0508-5

Huang C-S, Foster JC, Kelley MC (2005) Long-duration penetration of the interplanetary electric field to the low-latitude ionosphere during the main phase of magnetic storms. J Geophys Res 110:A11309. doi:10.1029/2005JA011202

Huba JD, Sazykin S (2014) Storm time ionosphere and plasmasphere structuring: SAMI3-RCM simulation of the 31 March 2001 geomagnetic storm. Geophys Res Lett 41(23):8208–8214. doi:10.1002/2014GL062110

Jakowski N, Jungstand A, Schlegel K, Kohl H, Rinnert K (1992) The ionospheric response to perturbation electric fields during the onset phase of geomagnetic storms. Can J Phys 70(7):575–581. doi:10.1139/p92-093

Jin SG, Luo OF, Park P (2008) GPS observations of the ionospheric F2-layer behavior during the 20th November 2003 geomagnetic storm over South Korea. J Geod 82(12):883–892. doi:10.1007/s00190-008-0217-x

Jin SG, Jin R, Li JH (2014) Pattern and evolution of seismo-ionospheric disturbances following the 2011 Tohoku earthquakes from GPS observations. J Geophys Res Space Phys 119(9):7914–7927. doi:10.1002/2014JA019825

Jin SG, Occhipinti G, Jin R (2015) GNSS ionospheric seismology: recent observation evidences and characteristics. Earth-Sci Rev 147:54–64. doi:10.1016/j.earscirev.2015.05.003

Jin SG, Jin R, Li D (2016) Assessment of BeiDou differential code bias variations from multi-GNSS network observations. Ann Geophs 34(2):259–269. doi:10.5194/angeo-34-259-2016

Klimenko MV, Klimenko VV, Ratovsky KG, Goncharenko LP (2012) Numerical modeling of the global ionospheric effects of storm sequence on September 9–14, 2005–comparison with IRI model. Earth Planets Space 64:433–440. doi:10.5047/eps.2011.06.048

Kil H, Kwak YS, Paxton LJ, Meier RR, Zhang Y (2011) O and N2 disturbances in the F region during the 20 November 2003 storm seen from TIMED/GUVI. J Geophys Res: Space Phys. doi:10.1029/2010JA016227

Lei J, Wang W, Burns AG, Solomon SC, Richmond AD, Wiltberger M, Goncharenko LP, Coster A, Reinisch BW (2008) Observations and simulations of the ionospheric and thermospheric response to the December 2006 geomagnetic storm: Initial phase. J Geophys Res: Space Phys. doi:10.1029/2007JA012807

Lei J, Wang W, Burns AG, Yue X, Dou X, Luan X, Solomon SC, Liu YCM (2014) New aspects of the ionospheric response to the october 2003 superstorms from multiple-satellite observations. J Geophys Res: Space Phys 119(3):2298–2317. doi:10.1002/2013JA019575

Liu J, Zhao B, Liu L (2010) Time delay and duration of ionospheric total electron content responses to geomagnetic disturbances. Ann Geophys 28(3):795–805. doi:10.5194/angeo-28-795-2010

Liu S-L, Li L-W (2002) Study on relationship between Southward IMF events and geomagnetic storms. Chin J Geophys 45(3):301–310. doi:10.1002/cjg2.243

Mangla B, Sharma DK, Rajput A (2014) Diurnal and seasonal variation of topside ionospheric ion density over Indian region at solar minimum and solar maximum. Adv Space Res 54(9):1813–1817. doi:10.1016/j.asr.2014.07.031

Mannucci AJ, Tsurutani BT, Iijima BA et al (2005) Dayside global ionospheric response to the major interplanetary events of October 29–30, 2003 "Halloween Storms". Geophys Res Lett 32:L1S02. doi:10.1029/2004GL021467

Martyn DF (1953) The morphology of the ionospheric variations associated with magnetic disturbance. I. Variations at moderately low latitudes. Proc R Soc Lond A: Math Phys Eng Sci 218(1132):1–18. doi:10.1098/rspa.1953.0082

Matsushita S (1959) A study of the morphology of ionospheric storms. J Geophys Res 64(3):305–321. doi:10.1029/JZ064i003p00305

Mendillo M (1971) Ionospheric total electron content behaviour during geomagnetic storms. Nat Phys Sci 234:23–24. doi:10.1038/physci234023a0

Mendillo M (2006) Storms in the ionosphere: patterns and processes for total electron content. Rev Geophys 44(4):RG4001. doi:10.1002/2013JA019692

Mikhailov AV, Förster M (1997) Day-to-day thermosphere parameter variation as deduced from Millstone Hill incoherent scatter radar observations during March 16–22, 1990 magnetic storm period. Ann Geophys 15(11):1429–1438. doi:10.1007/s00585-997-1429-8

Nava B, Rodríguez-Zuluaga J, AlazoCuartas K, Kashcheyev A, Migoya-Orué Y, Radicella SM, Amory-Mazaudier C, Fleury R (2016) Middle- and low-latitude ionosphere response to 2015 St. Patrick's Day geomagnetic storm. J Geophys Res Space Phys. doi:10.1002/2015JA022299

Prölss GW (1995) Ionospheric F-region storms. In: Volland H (ed) Handbook of atmospheric electrodynamics, 2nd edn. CRC Press, Boca Raton, Fla., pp 195–248

Richards PG (2001) Seasonal and solar cycle variations of the ionospheric peak electron density: comparison of measurement and models. J Geophys Res: Space Phys 106(A7):12803–12819. doi:10.1029/2000JA000365

Richardson IG, Cane HV (2012) Solar wind drivers of geomagnetic storms during more than four solar cycles. J Space Weather Space Clim 2:A01. doi:10.1051/swsc/2012001

Richardson IG (2013) Geomagnetic activity during the rising phase of solar cycle 24. J Space Weather Space Clim. doi:10.1051/swsc/2013031

Sato T (1956) Disturbances in the ionospheric F2 region associated with geomagnetic storms I. Equatorial zone. J Geomagn Geoelectr 8(4):129–135. doi:10.5636/jgg.8.129

Seaton MJ (1956) A possible explanation of the drop in F-region critical densities accompanying major ionospheric storms. J Atmos Terr Phys 8(1):122–124. doi:10.1016/0021-9169(56)90102-7

Strickland DJ, Daniell RE, Craven JD (2001) Negative ionospheric storm coincident with DE 1-observed thermospheric disturbance on October 14, 1981. J Geophys Res: Space Phys 106(A10):21049–21062. doi:10.1029/2000JA000209

Tsai H-F, Liu J-Y, Tsai W-H, Liu C-H, Tseng C-L, Wu C-C (2001) Seasonal variations of the ionospheric total electron content in Asian equatorial anomaly regions. J Geophys Res: Space Phys 106(A12):30363–30369. doi:10.1029/2001JA001107

Tulasi Ram S, Yokoyama T, Otsuka Y et al (2016) Duskside enhancement of equatorial zonal electric field response to convection electric fields during the St. Patrick's Day storm on 17 March 2015. J Geophys Res Space Phys 121:538–548. doi:10.1002/2015JA021932

Vijaya Lekshmi D, Balan N, Tulasi Ram S, Liu JY (2011) Statistics of geomagnetic storms and ionospheric storms at low and mid latitudes in two solar cycles. J Geophys Res: Space Phys 116:A11328. doi:10.1029/2011JA017042

Wang W, Lei J, Burns A, Solomon S, Wiltberger M, Xu JJ, Coster A (2010) Ionospheric response to the initial phase of geomagnetic storms: common features. J Geophys Res: Space Phys 116:11328. doi:10.1029/2009JA014461

Yue X, Wang W, Lei J, Burns A, Zhang Y, Wan W, Liu L, Hu L, Zhao B, Schreiner WS (2016) Long-lasting negative ionospheric storm effects in low and middle latitudes during the recovery phase of the 17 March 2013 geomagnetic storm. J Geophys Res: Space Phys 121:9234–9249. doi:10.1002/2016JA022984

Zhang Y, Paxton LJ, Morrison D, Wolven B, Kil H, Meng CI, Mende SB, Immel TJ (2004) O/N2 changes during 1–4 October 2002 storms: IMAGE SI-13 and TIMED/GUVI observations. J Geophys Res: Space Phys 109(A10):A10308. doi:10.1029/2004JA010441

Zhao B, Wan W, Liu L, Igarashi K, Yumoto K, Ning B (2009) Ionospheric response to the geomagnetic storm on 13–17 April 2006 in the West Pacific region. J Atmos Solar Terr Phys 71(1):88–100. doi:10.1016/j.jastp.2008.09.029

Zhao X, Jin SG, Mekik C, Feng J (2016) Evaluation of regional ionospheric grid model over China from dense GPS observations. Geod Geodyn 7(5):361–368